

# The 2011 $M_w$ 5.2 Lorca earthquake as a case study to investigate the ground motion variability related to the source model

Luca Moratto<sup>1</sup>  · Angela Saraò<sup>2</sup> · Alessandro Vuan<sup>2</sup> · Marco Mucciarelli · María-José Jiménez<sup>3</sup> · Mariano García-Fernández<sup>3</sup>

Received: 14 July 2016 / Accepted: 16 February 2017 / Published online: 3 March 2017  
© Springer Science+Business Media Dordrecht 2017

**Abstract** Near-field recordings are very sensitive to the spatiotemporal details of the rupture process while far-field signals show the signature of the overall “point-source” earthquake mechanism. Near- and far-field recording ranges are dependent on the event magnitude and modulate the variability of the ground motion. This study investigates the ground motion and the source-related near-field variability for the 2011 Lorca earthquake, a moderate seismic event ( $M_w = 5.2$ ) that caused significant localized damage in the Region of Murcia, Spain. The low-frequency content (up to 1 Hz) is simulated by the wavenumber integration method assuming four different source models obtained by inversion of geodetic or seismological data. As a first result, we estimate the variability of the ground motion. We observe that the dispersion in the peak and spectral parameters is larger at LOR, the closest station to the source, and decreases as the source distance increases (more than 50 km far from the source) where the finite-fault effects become negligible. The variability of the pseudo spectral velocity at 2 s is within the ground motion prediction equation  $\pm 1 \sigma$ , apart from the very near-source station and those stations affected by forward directivity effects. These effects are also found in high-frequency seismograms obtained by the empirical Green’s functions approach.

**Keywords** Lorca earthquake · Synthetic seismograms · Empirical Green Functions · Ground motion variability · Source effects · Rupture directivity · Near-source

---

Marco Mucciarelli: deceased 7 November 2016.

---

✉ Luca Moratto  
lmoratto@inogs.it

<sup>1</sup> Centro di Ricerche Sismologiche, Istituto Nazionale di Oceanografia e di Geofisica Sperimentale - OGS, v. Treviso 55, 33100 Udine, Italy

<sup>2</sup> Centro di Ricerche Sismologiche, Istituto Nazionale di Oceanografia e di Geofisica Sperimentale - OGS, Borgo Grotta Gigante 42c, 34010 Sgonico, Trieste, Italy

<sup>3</sup> Consejo Superior de Investigaciones Científicas, MNCN-CSIC, José Gutiérrez Abascal 2, 28006 Madrid, Spain

## 1 Introduction

On 11 May 2011 at 16:47 UTC, an  $M_w$  5.2 earthquake shook the town of Lorca in south-eastern Spain (Fig. 1a), nearly 2 h after an  $M_w$  4.5 foreshock. The epicenter was located 5 km northeast (NE) of Lorca and at a shallow depth (around 4 km). Despite its moderate magnitude, the event caused nine fatalities, and more than 300 people were injured in a town with a population of around 60,000 in an area of 7 km<sup>2</sup>. The city suffered relevant damage reaching a ground-shaking intensity of EMS VII. More than 1000 buildings, including residential housing, schools, healthcare and security facilities, government establishments and cultural heritage monuments, were severely damaged. However, nearby towns and provinces were not severely affected.

The 2011 seismic sequence lasted for more than 2 months, with about 140 aftershocks (López-Comino et al. 2012; Pro et al. 2014): the strongest aftershock ( $M_w = 3.9$ ) occurred 4 h after the mainshock. The correlation between the mainshock and the causative active fault is not straightforward because the tectonic structure is represented by a complex fault system with a branched geometry (Martínez-Díaz et al. 2012); furthermore, no surface rupture was observed (Frontera et al. 2012; Martínez-Díaz et al. 2012). Most of the authors (e.g. López-Comino et al. 2012) locate the mainshock on the Alhama de Murcia fault (AMF) system, principally connected with the Europe-Africa motion, which runs in an NNE–SSW direction for 100 km in the eastern Betic Cordillera (Fig. 1a). Pro et al. (2014) associate the 2011 earthquake to a parallel fault, Cejo de los Enamorados (CE), located a few kilometers to the northwest of the city of Lorca, in the Neogene Lorca basin (Fig. 1a). The only near-fault accelerometer (LOR) is located in the Lorca city and recorded, in the horizontal component perpendicular to the AMF, the strongest peak ground acceleration ( $PGA = 360 \text{ cm/s}^2$ ) ever observed in Spain.

Several authors investigated the possible effects related to the seismic source (e.g., González et al. 2012; López-Comino et al. 2012; Martínez-Díaz et al. 2012; Pro et al. 2014; Rueda et al. 2014; Santoyo 2014) and local soil amplification (Navarro et al. 2014).

To date, all the aforementioned studies agree on the fact that the relatively large acceleration recorded at LOR, the nearest station to the epicenter (Table 1 and Fig. 1a), could be associated to rupture directivity effects and no evidence of significant local site effects has been found (e.g., Alguacil et al. 2014). Thus, the major damage experienced in the city of Lorca is very likely the result of the strong motion due to the directivity effect combined with differentiated vulnerability levels of buildings (e.g., Beltrán Díez et al. 2013; Rivas-Medina et al. 2014).

González et al. (2012) relate the strong ground motion recorded in Lorca to a very shallow slip distribution controlled by crustal unloading stresses at the upper frictional transition of the seismogenic layer, possibly induced by groundwater extraction during the last 50 years. Also, Martínez-Díaz et al. (2012) observed, through interferometry data, a deformation southeast of the AMF that they associate with these long-term groundwater extractions. However, Avouac (2012) questions that correlation, because the elastic stresses released during the earthquake were orders of magnitude larger than those induced by groundwater unloading; so, any correlation could be entirely fortuitous.

The existence of various source models for this moderate magnitude earthquake allows us for investigating the ground motion variability related to the source parameterization. It is very well known (e.g., Mai et al. 2010) that the variability of ground motion is determined by source, path, and site effects and multiple equivalent source models exist for one moderate or large earthquake (Mai and Thingbaijam 2014). The source models are

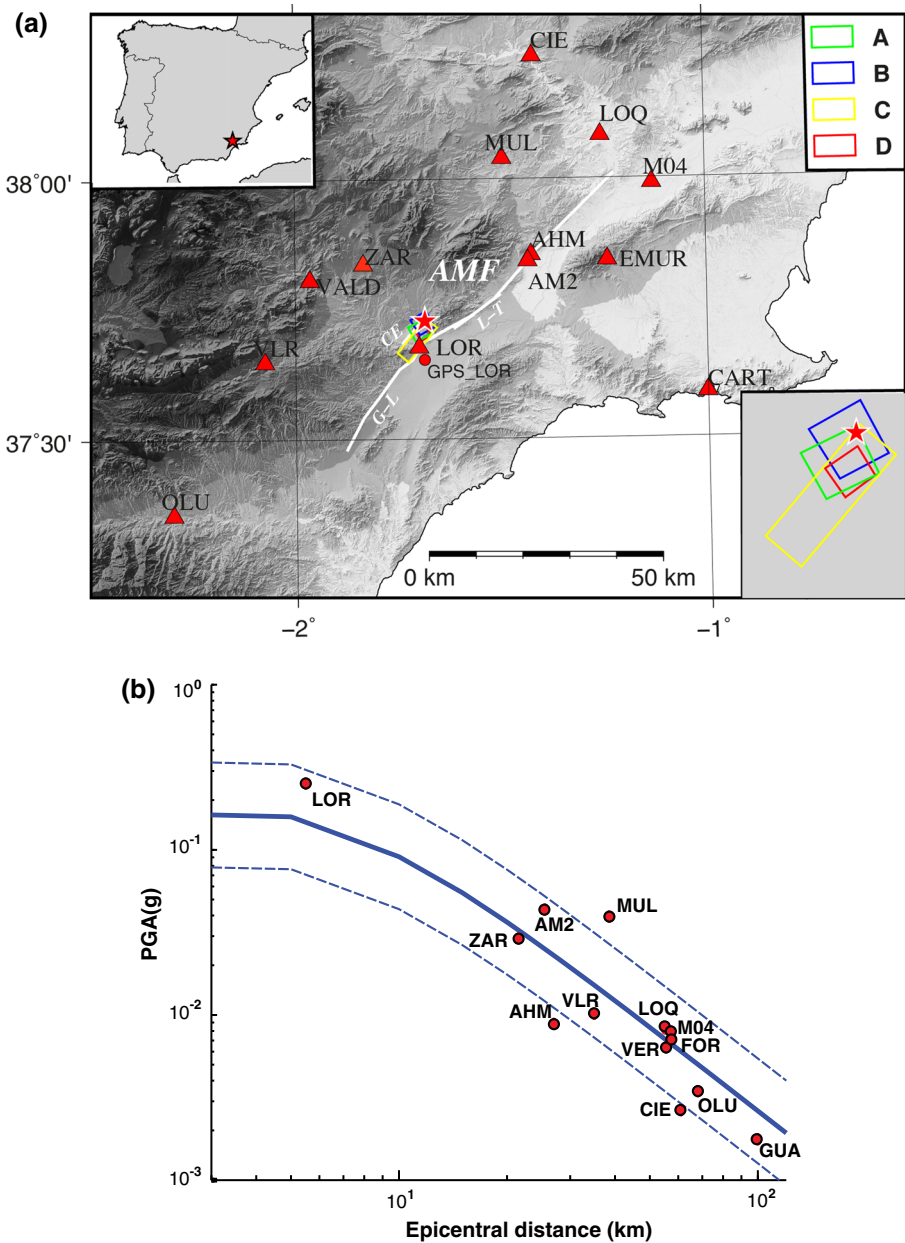


**Fig. 1** **a** Map of the Lorca mainshock (red star) and of the main faults mentioned in the text: Alhama de Murcia fault (AMF), Goñar–Lorca segment (G–L), Lorca–Totana segment (L–T), Cejo de los Enamorados (CE). The 13 stations (red triangles) considered in this study and the GPS station (red circle) are also plotted. The lower corner inset zooms the surface projection of the four fault boxes used in the modeling. **b** PGA values as a function of the epicentral distance; the solid line shows the median PGA estimated by applying the GMPE proposed by Akkar et al. (2014) for a reverse fault and a reference  $V_{s30} = 750$  m/s, while the dotted lines represent the associated uncertainty bounds

**Table 1** Accelerometric stations that recorded the 2011 Lorca mainshock

Station name	Station code	N latitude	W longitude	H (m)	PGA (cm/s <sup>2</sup> )		
					NS	Vert	EW
Lorca <sup>a</sup>	LOR	37.6767°	−1.7002°	360	359.96	115.08	150.6
Zarcilla de Ramos	ZAR	37.8446°	−1.8779°	653	35.15	26.19	31.99
Alhama de Murcia Polideportivo	AM2	37.8415°	−1.4344°	200	42.95	24.66	45.96
Alhama de Murcia Biblioteca	AHM	37.8531°	−1.4258°	202	9.86	9.15	7.65
Vélez-Rubio	VLR	37.6483°	−2.0745°	848	10.76	5.97	9.32
Mula	MUL	38.0396°	−1.4941°	315	35.88	20.21	41.63
Vera	VER	37.2522°	−1.8705°	102	5.49	4.95	7.05
Lorquí	LOQ	38.0825°	−1.2534°	115	8.19	4.06	8.13
Murcia	M04	37.9899°	−1.1296°	70	7.17	3.46	8.36
Cieza	CIE	38.2364°	−1.4181°	170	2.39	1.37	2.72
Olula del Rio	OLU	37.3537°	−2.2974°	94	2.57	1.82	4.62
Fortuna	FOR	38.1828°	−1.1272°	235	6.39	3.47	7.38
Guardamar del Segura	GUA	38.0950°	−0.6584°	20	2.02	0.77	1.43

<sup>a</sup> Horizontal channels are oriented E30N and N30W instead of EW and NS

sensitive to the data used, to the chosen inversion technique, and to the model parameterization: global positioning system (GPS) and interferometric synthetic aperture radar (InSAR) data actually can constrain the seismic moment and the fault geometry, but they have limited resolution for the dip slip and the high frequencies in the range of engineering interest; teleseismic data usually give a fairly well resolution for the overall rupture, but for rupture details on relatively fine space–time scales, near-fault strong-motion data are definitely needed. Additionally, in this last case, the slip inversion is strongly affected by data distribution and wave propagation (Mai and Thingbaijam 2014). Ideally, the different source models should predict identical ground motions. However, the uncertainties in kinematic inversions (including both epistemic uncertainty and aleatory variations) manifest themselves in intraevent ground motion variability (Vyas et al. 2016). The lack of near-field recordings obstructs a complete understanding of the physical causes of such variability. Hence, well constrained physical modeling of ground motion, which includes complex rupture processes and wave-propagation effects, could be instrumental in providing useful insights (e.g., Spudich and Frazer 1984; Ripperger et al. 2008; Mai et al. 2010; Vyas et al. 2016).

In this study we compute the ground motion (up to 1 Hz) of the 2011 Lorca earthquake, a moderate event of  $M_w = 5.2$ , using four published source models obtained from inversion of geodetic and seismological data. It is beyond the scope of this article to validate the models or to discuss the uncertainties related to specific fault parameters in detail. Our main goal is to investigate the ground motion variability from the different source models and to compare it with that estimated from the ground motion prediction equation (GMPE). As a final step, we compute synthetic high-frequency seismograms (up to 20 Hz) using the empirical Green functions approach and the low-frequency best-fitting source model to reproduce the observations in the near-field.

## 2 The recorded data

The 2011 Lorca mainshock was recorded by a number of accelerometric stations run by the Instituto Geográfico Nacional (IGN); 13 of them were within 100 km of the source, six of which (LOR, ZAR, AM2, AHM, VLR, and MUL) are located at less than 50 km (Table 1; Fig. 1a). These stations have principally the accelerometers GeoSIG GSR 18 (18-bit resolution), which incorporate force balance sensors and flat response in acceleration (Cabañas et al. 2014); the sampling frequency is 200 Hz.

Most of the available studies on the Lorca 2011 earthquake (e.g., González et al. 2012; López-Comino et al. 2012; Martínez-Díaz et al. 2012; Pro et al. 2014; Rueda et al. 2014) highlight the apparent exceptional nature of the ground motion produced by this event, and its possible relation to the extensive damage observed. According to Anderson (2010), ground motions can be considered exceptional if  $PGA > 500 \text{ cm/s}^2$  and peak ground velocity  $PGV > 50 \text{ cm/s}$  on at least one component. This is not the case for the maximum recorded ground motion at the station LOR. In fact, most of the recorded PGA values, including LOR, are within the  $\pm\sigma$  variability range predicted by updated ground-motion prediction equations like, e.g., Akkar et al. (2014) (Fig. 1b).

The original LOR record includes a spike at around 5 s from the origin time (Fig. 2a), which is also very visible in frequency domains (Fig. 2b). The spike, due to an accidental fall of a metal bar hitting the pillar, was removed by applying a frequency-time analysis filter (Mucciarelli 2014). Furthermore, since the LOR accelerometer was placed on a pillar close to a thick wall (Fig. 3a), we simultaneously performed 1-hour noise measurements using three Tromino<sup>®</sup> seismic sensors to discard any effects associated with the installation of the equipment. The sensors were placed on the top and the bottom of the pillar and next to the wall (Fig. 3a). We then computed the horizontal average H/V ratios separately from the recorded noise. The results (Fig. 3b) show no significant amplification effects in the recorded noise for frequencies lower than 15 Hz, i.e., the full frequency range simulated by our synthetics. Also, the pillar and the wall seem to have no influence on the recordings, even if all these considerations apply only in the case of weak motion.

The GPS data recorded at the LORC station, about 2 km south of LOR, show an amplitude of the signal, defined as half of the peak-to-peak displacement,  $\sim 1.5 \text{ cm}$  for N–S,  $\sim 0.8 \text{ cm}$  in E–W (Mendoza et al. 2012). To compare the near-field ground motion from two different types of observations, we differentiated the GPS time series and made it comparable with the filtered accelerograms recorded at LOR (Fig. 4). The two different types of signals were filtered in the range 0.01–0.05 Hz to reduce the effect of wave propagation in the LOR signal. A similar comparison for seismic displacement was carried out by Pro et al. (2014). In both cases, the GPS data are consistent with the strong motion data, confirming the absence of strong site effect and the presence of mainly rupture directivity effects.

## 3 Modeling of low-frequency strong ground motion

We computed the low-frequency ground motion (up to 1 Hz) applying the discrete wavenumber technique used by COMPSYN (Spudich and Xu 2003), a widely used and validated approach (e.g. Ripperger et al. 2008; Ameri et al. 2008; Moratto et al. 2015) for an elastic medium. The 1D velocity model is taken from the study of Corchete and Chourak (2011) for the Southeastern Iberian peninsula (Table 2). We assumed that the

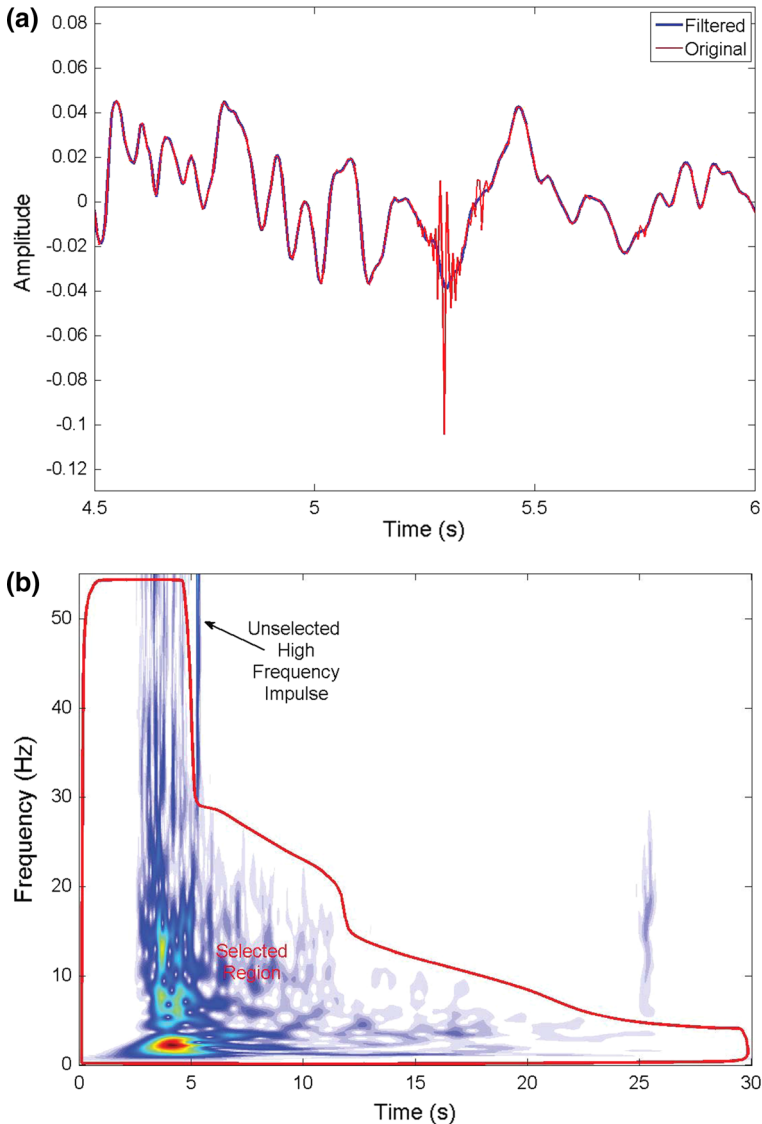


**Fig. 2** **a** Acceleration recorded at LOR (Amplitude in  $m/s^2$ ) **b** selective frequency–time analysis applied to the horizontal component acceleration record (LOR E30N) for removing the spike at around 5 s

receivers (see Fig. 1a; Table 1) are located on rock since no specific station-site information about soil characteristics is available (Cabañas et al. 2014). The seismic source is represented as a box fault adopting a kinematic model with constant rise time and constant velocity rupture; the source time function is parameterized by a regularized Yoffe function (e.g. Tinti et al. 2005). We modeled four scenarios, changing the fault geometry, the slip distribution, and the rupture velocity to reproduce four source models (Table 3; Fig. 5) proposed in the literature. We classified the unilateral and bilateral rupture through the directivity ratio computed according to the McGuire et al. (2002). All the models

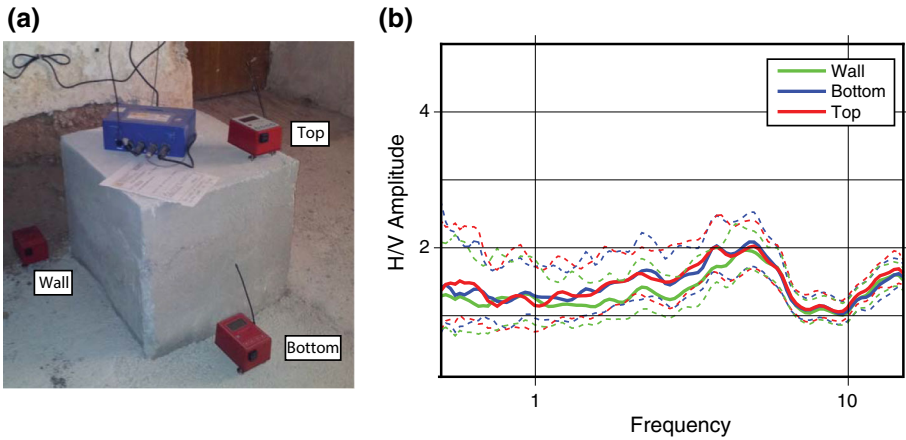


**Fig. 3** **a** LOR accelerometer (blue box) on top of the pillar, and the three Tromino<sup>®</sup> instruments (red boxes) placed near to the wall, at the bottom and on the top of the pillar; **b** ambient-noise H/V ratios (solid line) and 95% confidence interval about the H/V amplitude ratio (dotted line)

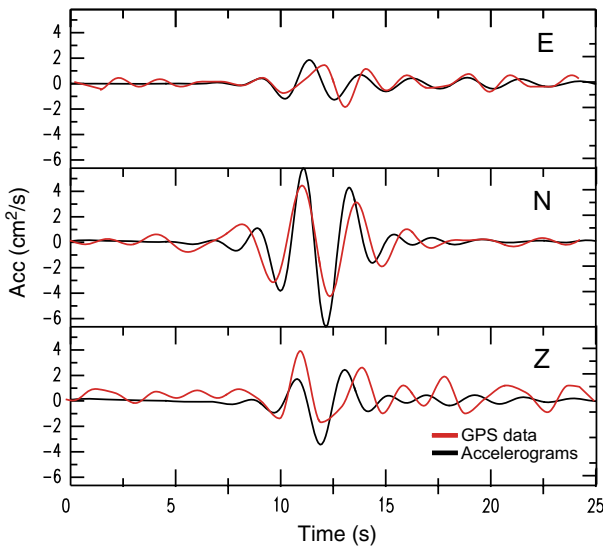


**Fig. 4** Comparison of the LOR accelerograms and GPS data recorded at Lorca. The high-gain GPS data have been differentiated twice to make them comparable with the recorded seismograms

considered share a very similar epicentral location (about 4–5 km NE of Lorca) and focal mechanisms. Inversion procedures commonly overestimate source sizes so that the entire rupture can be accommodated. Thus, we trimmed unnecessary zero slip stripes at the fault edges, and we discretized the fault plane using a bilinear interpolation to obtain the grid resolution as a function of the maximum frequency used in the time series computation.

Details of the different models, together with the results of our modeling, are given in what follows. To validate our approach, we first compare the simulated waveforms with the records at the stations located within 50 km from the epicenter.

**Table 2** 1D velocity model retrieved from Corchete and Chourak (2011)

Depth (km)	Density (g/cm <sup>3</sup> )	Vp (km/s)	Vs (km/s)
0.0	2.10	4.50	2.60
2.0	2.40	5.20	3.10
5.0	2.40	5.40	3.20
10.0	2.80	6.12	3.60
25.0	2.80	6.57	3.80
35.0	2.90	7.76	4.50

**Table 3** Source parameters used in this study

Parameter	Model A Martínez-Díaz et al. (2012)	Model B Santoyo (2014)	Model C González et al. (2012)	Model D Rueda et al. (2014)
Data inverted	InSAR data	LOR strong motion data	InSAR + GPS data	Seismological data
Hypo LatN, LongW	37.727°–1.686°	37.727°–1.686°	37.727°–1.686°	37.718°–1.677°
Hypo depth (km)	4.5	4.5	4.0	4.0
Moment magnitude ( $M_w$ )	5.2	5.2	5.1	5.2
FPS (strike, dip rake)	235°, 55°, 39°	240°, 55°, 45°	225°, 70°, 36°	230°, 64°, 37°
Fault dimension (L × W)	4.0 × 3.0	4.0 × 4.0	8.0 × 5.0	3.7 × 3.8
Velocity rupture (km/s)	2.4	2.4	2.4	1.8
Directivity ratio	0.70	0.75	0.95	0.95
Rise time (s)	0.15	0.15	0.15	0.15

**Model A** It is based on the source model proposed by Martínez-Díaz et al. (2012), who used radar interferometry to investigate the co-seismic deformation. The authors merged these data with the results published by López-Comino et al. (2012), who studied the 2011 Lorca seismic sequence using seismic data. In their model, the rupture propagated toward southwest (SW) within an area of  $\sim 4 \text{ km}^2 \times 3 \text{ km}^2$  within the complex structure that limits the Goñar–Lorca (G–L) and Lorca–Totana (L–T) segments of the AMF (Fig. 1a). The co-seismic slip distribution was concentrated in a zone of about  $3 \text{ km}^2 \times 3 \text{ km}^2$ , with a maximum slip of 15 cm and a mean of about 7 cm; a moderate level of slip ( $\sim 4$  cm) occurred near the mainshock nucleation. The computed waveforms obtained using Model A (Fig. 5) underestimate the ground motion recorded on the North component of LOR (Fig. 6a) and at stations AM2, MUL, and ZAR (Fig. 7a), but are in good agreement with the amplitudes observed at AHM and VLR (Fig. 7a).

**Model B** This model is obtained by the waveform inversion of Santoyo (2014), who used only the signals recorded at LOR to avoid path and site effects observed at other stations (ZAR and AM2). In this model, the hypocenter coordinates and the focal

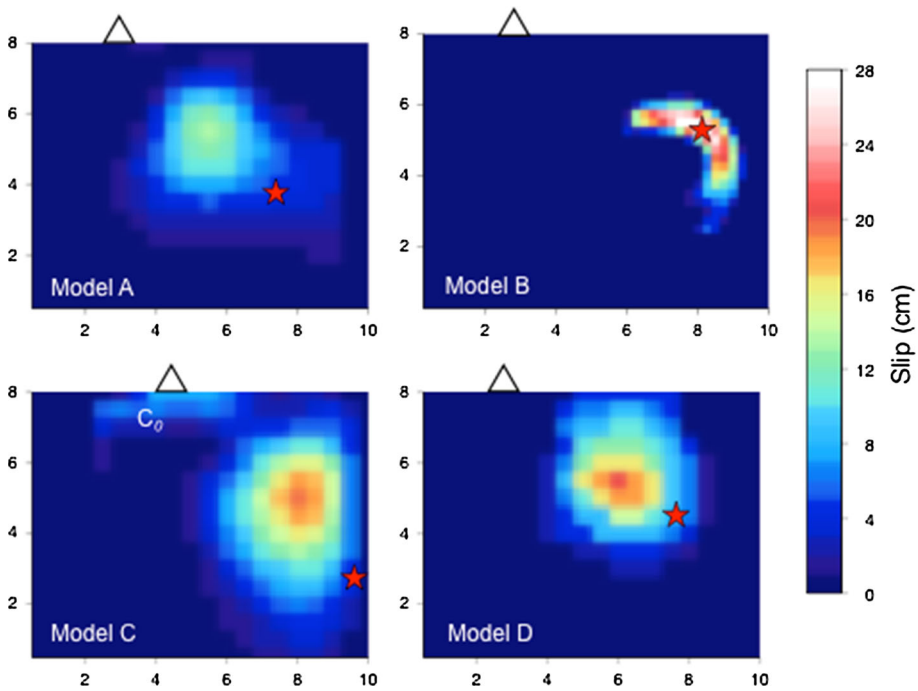


**Fig. 5** Fault boxes and slip distributions related to the Model A (Martínez-Díaz et al. 2012), Model B (Santoyo 2014), Model C (González et al. 2012) and Model D (Rueda et al. 2014). The nucleation point (*red star*) and the LOR station (*white triangle*) are also represented in each model

mechanism were retrieved from López-Comino et al. (2012). The slip distribution, concentrated in a rupture area of  $4 \text{ km}^2 \times 4 \text{ km}^2$ , has two patches, with the main one centered at the hypocenter; the maximum slip is 23 cm, and the rupture propagates toward SW (Fig. 5). The computed waveforms show peak amplitudes larger than those observed at VLR, located to the SW, and AHM and AM2 to the NE of the source (Fig. 7b). Computed and observed peak amplitudes are comparable at MUL. However, this source model produces lower ground motion than observed at ZAR and underestimates the amplitude of the North component at LOR (Fig. 6b).

*Model C* González et al. (2012) used geodetic data to determine the surface deformation associated with the Lorca earthquake. In their model, the main slip area ( $\sim 15 \text{ cm}$ ), representing about 90% of the total seismic moment, was released at depths of 2–5 km, on a rupture plane along the Alhama de Murcia Fault. A second smaller slip patch of about 5 cm of maximum displacement was located at shallower depth beneath the city of Lorca (Fig. 5). The fault geometry is twofold, and the dip angle increases from depth ( $72^\circ$ ) to surface ( $90^\circ$ ). The vertical segment was introduced in the fault geometry to better fit the data (González et al. 2012). However, no evidence of two possible different asperities (related to two patches) was observed in the recorded seismograms. We performed a preliminary modeling for LOR by splitting the source model into two separate sub-sources: one dipping  $72^\circ$  with the bigger patch (Model C) and the other one dipping  $90^\circ$  (Model  $C_0$ ) with the smaller patch. The LOR synthetics obtained using Model C (red line) and  $C_0$  (green line) are compared with records in Fig. 6c. Model  $C_0$  seems to better reproduce the observed peak amplitude at LOR despite the out of phase peak on the E component (see

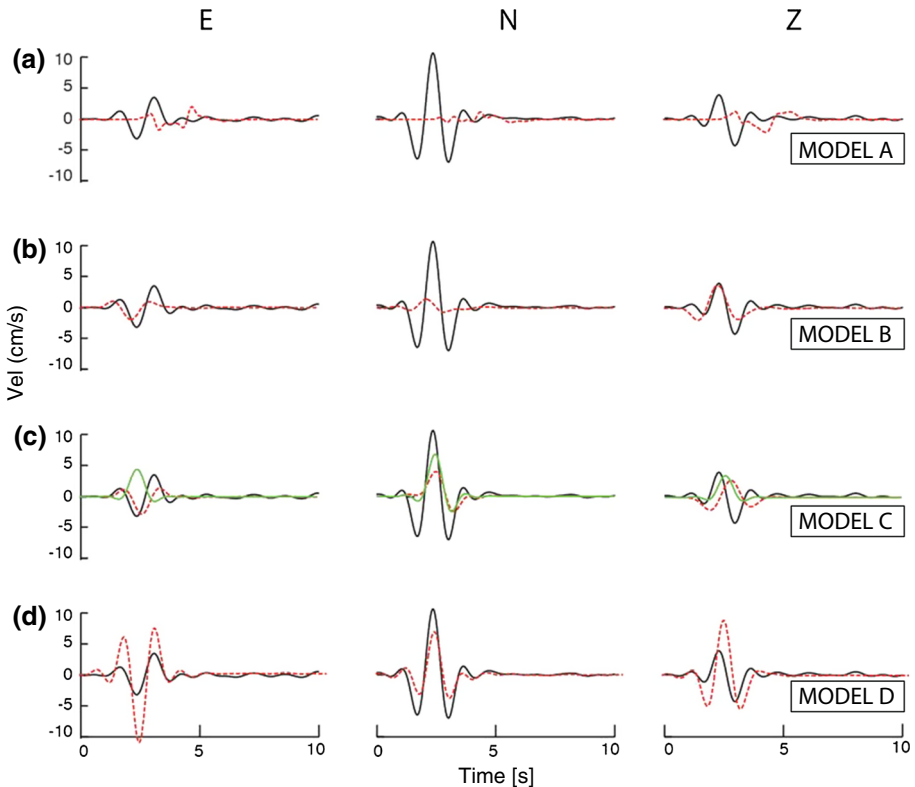


**Fig. 6** Comparison of recorded data (*black*) versus computed data (*red*) for the LOR station. The waveforms were computed adopting the following sources **a** Model A; **b** Model B; **c** Model C; **d** Model D. For case c, we also plot the waveforms (*green lines*) computed by considering only the small shallow patch ( $C_0$  in Model C of Fig. 5) along the vertical fault segment

Fig. 6c). To evaluate the sensitivity of the fault dip angle on our simulations, we computed the LOR synthetics considering Model  $C_0$ , but with a variable dip angle between  $45^\circ$  and  $90^\circ$ . Figure 8 shows that a dip angle of  $90^\circ$  generates a stronger signal on the transversal component compared to the radial one, which is in agreement with the observed data; this result validates the presence of a shallow slip patch on the vertical sub-fault proposed by González et al. (2012). However, source  $C_0$  works well only for LOR, and it provides a rather negligible effect on the other five stations. Therefore in Fig. 7c, and in the remaining study, we show only the synthetics computed using Model C.

**Model D** This model has obtained from Rueda et al. (2014), who inverted seismological data to retrieve the moment tensor and the slip distribution released by the earthquake; in their kinematic model, the rupture is unilateral propagating with a velocity of 1.8 km/s from the hypocenter towards SW. The slip distribution has a single asperity where the maximum value is 19.3 cm, with an average of 4.5 cm (Fig. 5). The synthetic seismograms are computed by adopting this source model, and the recorded signals are well reproduced in phase and amplitude at LOR (Fig. 6d) even though there are some discrepancies on the PGV values of the single motion components. Compared to A, B and C Models, the synthetics obtained from D fit better with the recorded signals at all selected stations (Fig. 7d). Further, the simulations are capable of fitting the first seconds of the signals

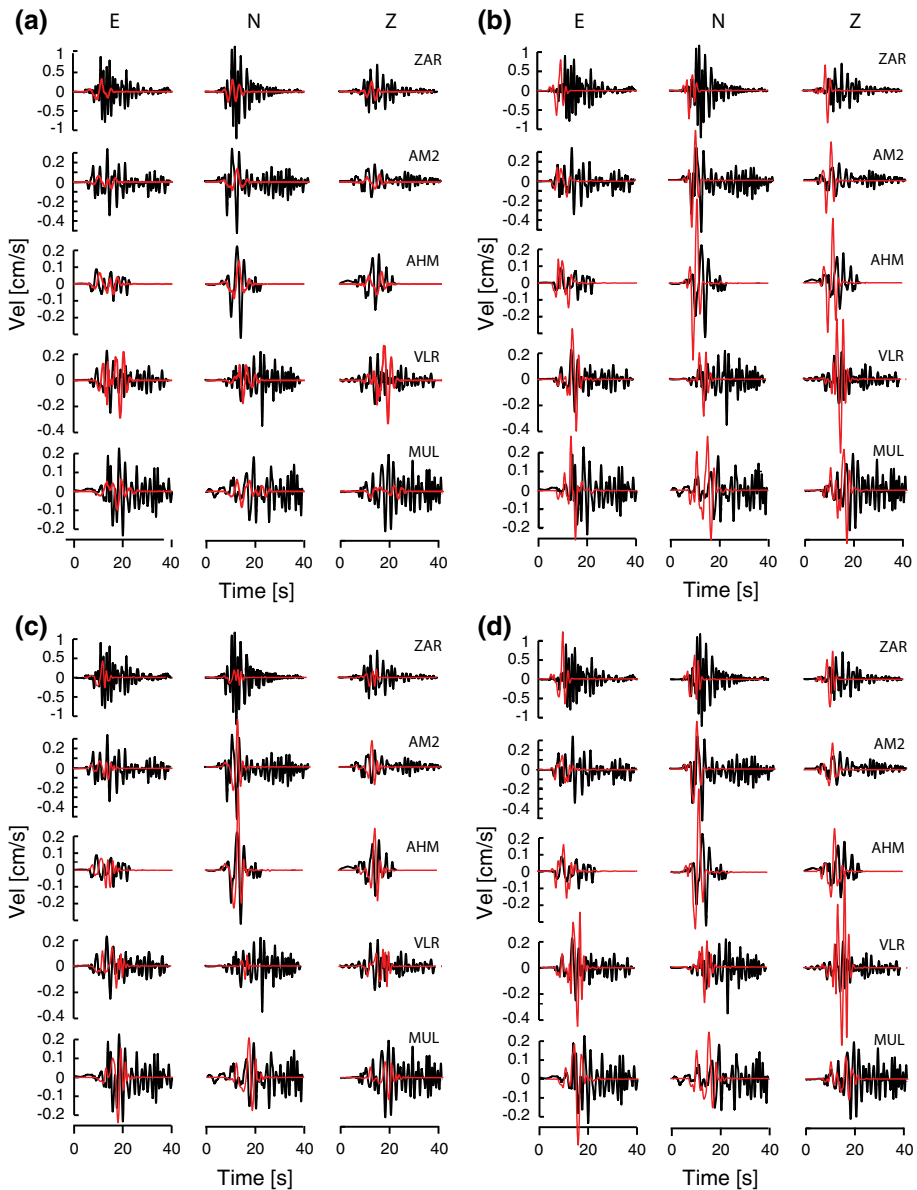


**Fig. 7** Comparison between the recorded velocities (*black lines*) and the velocity waveforms (*red lines*) computed at different stations utilizing the source **a** Model A; **b** Model B; **c** Model C; **d** Model D. The signals are filtered at an upper cutoff frequency of 1 Hz

when the duration of the recording is not well reproduced, probably related to site effects (Santoyo 2014) that are not considered in our simulations.

All the synthetics are then used to generate the ground-shaking maps in terms of PGV, which are obtained as the maximum velocity peak of the horizontal components (Fig. 9). The comparison with the real data map (Fig. 9a) shows that Model D (Fig. 9d) best fits the

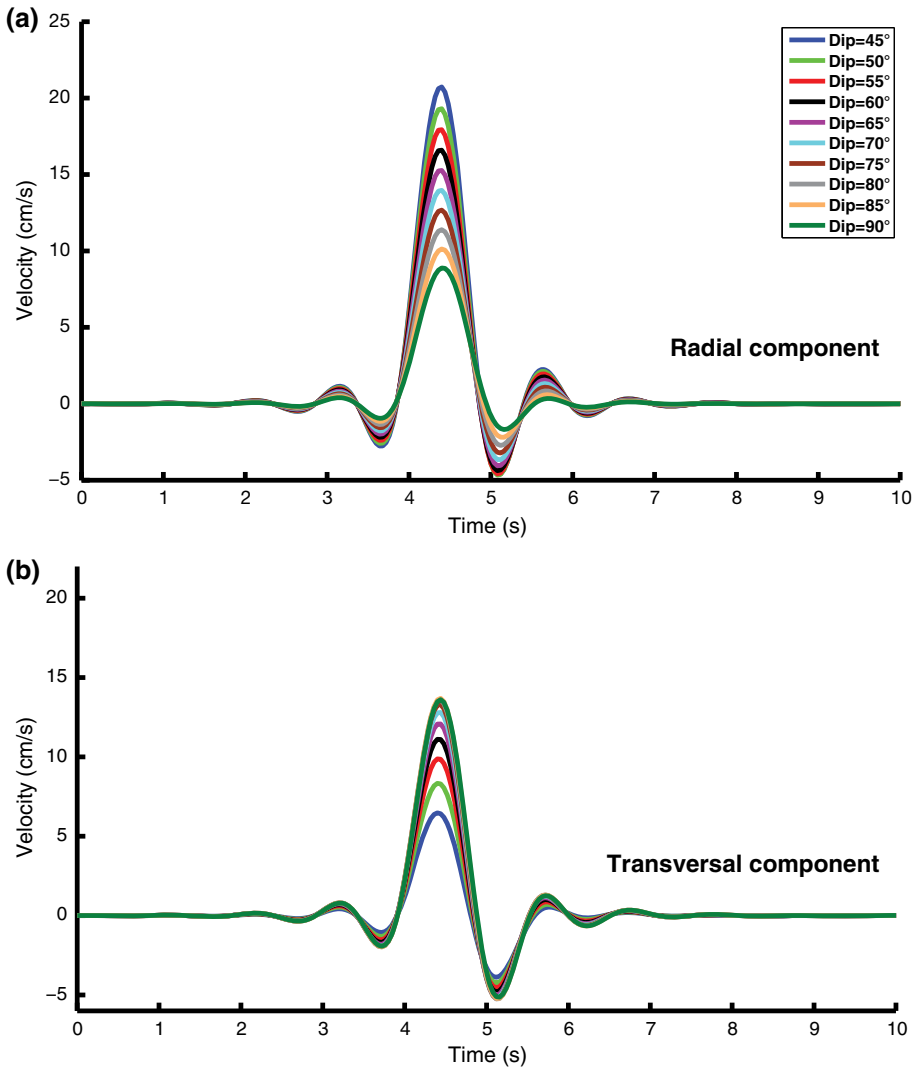


**Fig. 8** Comparison between the synthetics computed for radial and transversal components with different dip values at LOR site using only the patch  $C_0$  of source Model C

average level of PGV, especially in the near-fault area. In Fig. 10 we plot the 2 s pseudo spectral velocity (PSV) obtained for the four source models at each station as boxplots (Table 1) along the increasing distance from the fault; the red line of the boxes indicates the median value, while the box edges represent the 1st and 3rd quartiles. Because the directivity effects are evident in the frequency band ranging between 0.5 and 2 Hz and our waveforms are computed for an upper cutoff frequency of 1 Hz, we select the PSV at 2 s, obtained from both the horizontal components for each station, as a reference parameter. The 2 s PSV boxplots of Fig. 10 are compared with the GMPE values predicted by Akkar et al. (2014). We assume an uncertainty bound of  $\pm\sigma$  (see the gray area of Fig. 10). Akkar et al. (2014) PSV are retrieved from the PSA using the following relation  $PSV = PSA/(2\pi/$

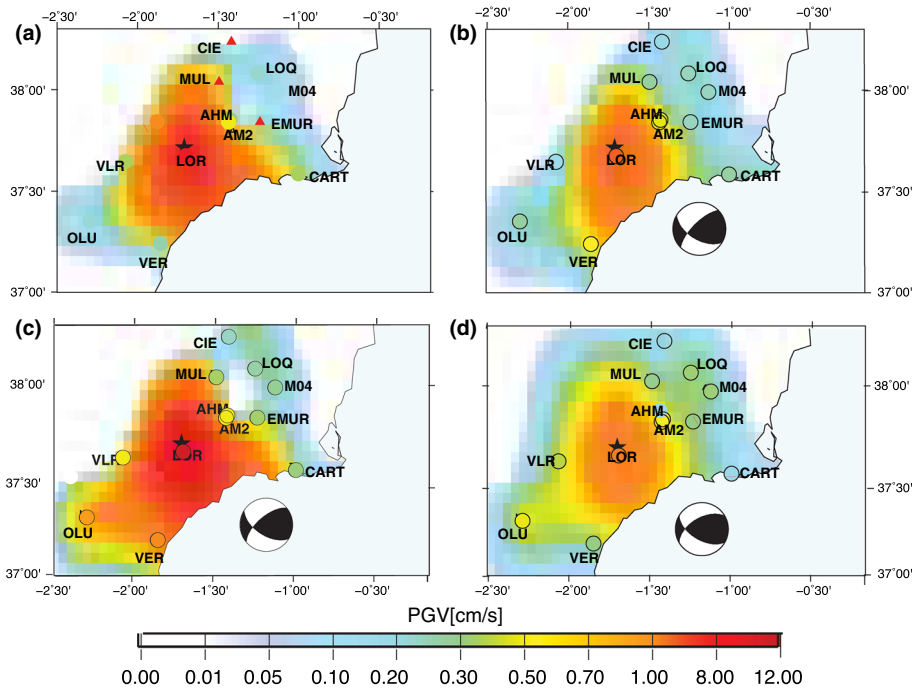


**Fig. 9** PGV shaking maps generated from **a** the real data and the waveforms computed by adopting the source **b** Model B, **c** Model C, and **d** Model D

T) with  $T = 2$  s. The dispersion of the PSV boxplot is larger at LOR and decreases as the source distance increases, in particular for the stations more than 50 km away from the source, where the finite-fault effects become negligible. On average, the scattering of the computed signals is comparable with that of the GMPE values except for the very-near-field region (LOR) and some stations (e.g., VER, OLU) located SW from the epicenter (Fig. 1a). Such discrepancy is due to the presence of strong directivity and rupture complexity, especially more in the very near-field, where GMPE could be biased by the lack of near-source strong motion records.

#### 4 Modeling of high-frequency strong ground motion

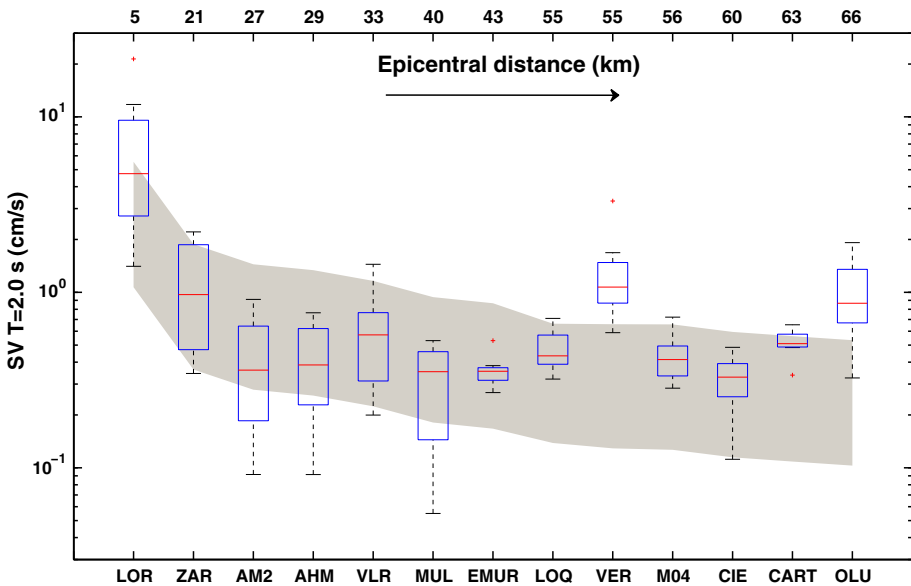
We apply the Empirical Green Functions (EGFs) approach proposed by Hartzell (1978) to compute high-frequency seismograms. In particular, we used the code developed by Miyake et al. (2003), based on a further development of the Irikura (1986) EGFs method: the waveforms for the mainshock (target earthquake) are computed by summing the recorded signals related to small aftershocks (element earthquakes), whose hypocenter and source mechanisms are very similar to the mainshock, and which are previously corrected through scaling laws. The source is represented as a finite fault with a constant velocity rupture (1.8 km/s), a constant rise time (0.15 s) and uniform seismic moment distribution; the nucleation must be fixed on the rupture area, and the directivity effects can be evaluated. The slip-velocity time function is adjusted by convolving it with a

**Fig. 11** Comparison between the recorded (black lines) and the EGF synthetic seismograms (red lines) computed for the **a** LOR **b** AM2 and **c** MUL stations; the source adopted is Model D

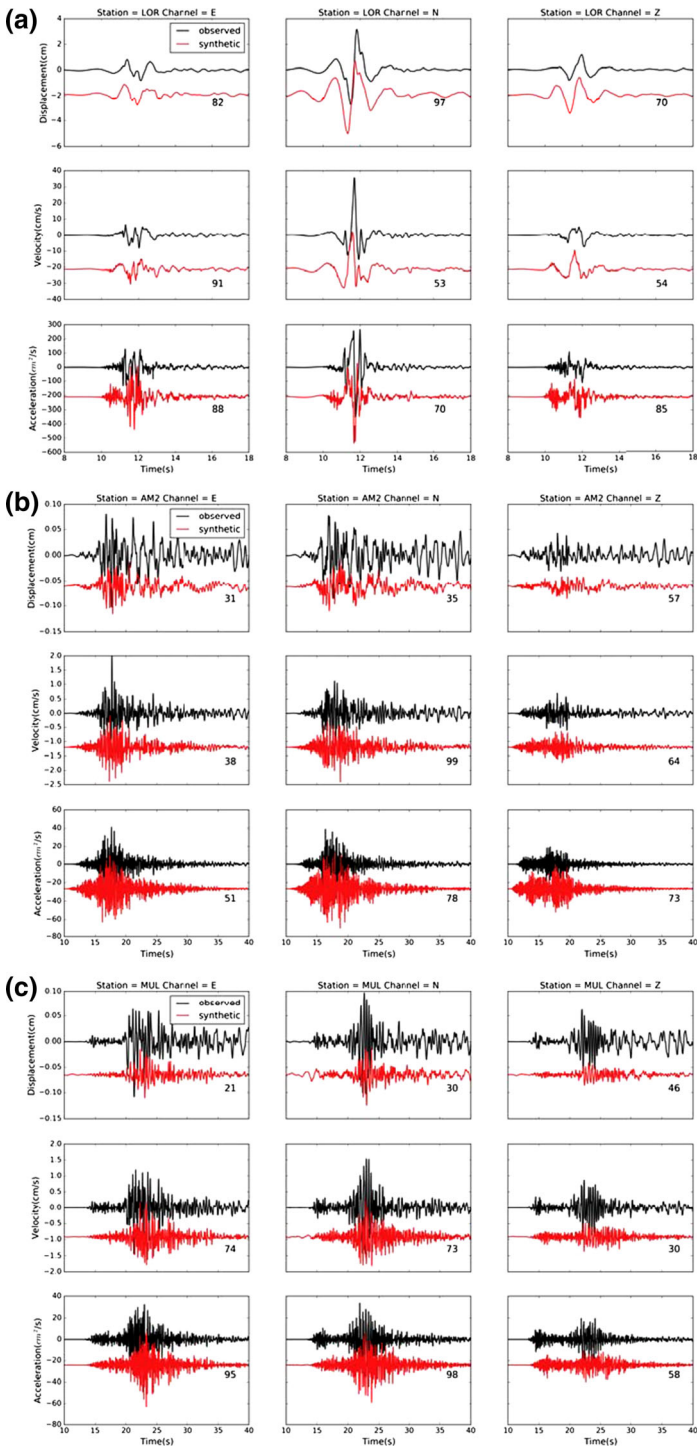
suitable correction filter represented by a delta function merged with an exponential decaying (Miyake et al. 2003). The ratio of the fault dimensions and the stress drop ratio between the mainshock and the aftershock can be specifically tuned by comparing the observed source spectra of the target and the element earthquake.

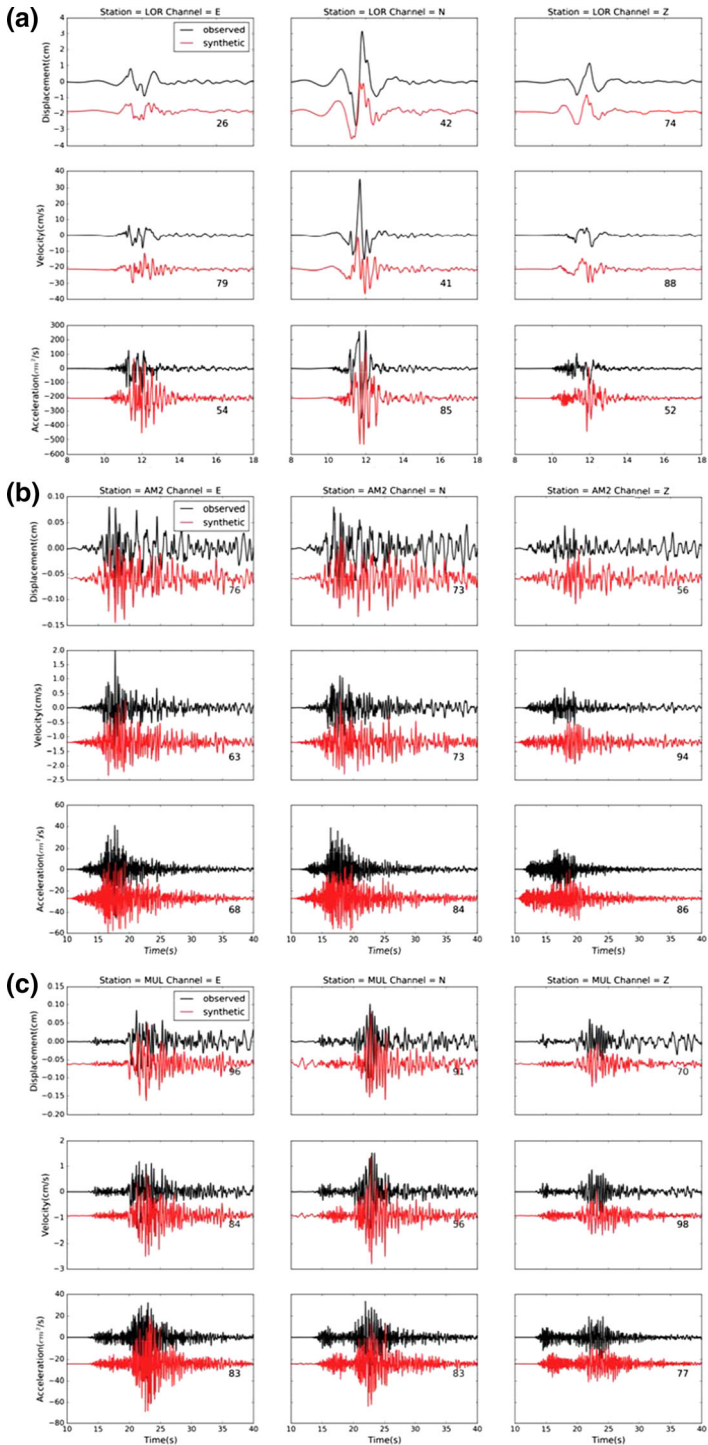
As the element earthquake, we select the strongest aftershock that occurred on 11 May 2011 (UTC 20:37;  $M_w = 3.9$ ), and it is the only one with all characteristics required for EGF simulations: the hypocenter is located very close to the mainshock, and the focal mechanism is very similar (strike = 215°; dip = 71°; rake = 39°). We utilize the Model D source with the rupture propagating almost unilaterally from NE to SW (Table 3); the rupture area is subdivided into  $10 \times 10$  cells, and the stress drop ratio between the mainshock and the aftershock is fixed to 1. We compute the synthetic seismograms in the frequency range 0.3–20.0 Hz at stations AM2, LOR, MUL, and ZAR, which were the only ones recording the aftershock among those located at distances less than 50 km. The goodness of fit (GOF) has been computed to compare the recorded and the simulated signals (Olsen and Mayhew 2010).

The LOR records (displacement, velocity, and acceleration) are reproduced well in amplitude, phase, and duration for all motion components (Fig. 11a); the fit is excellent ( $GOF = 70 \div 97$ ) for displacement and acceleration, fair ( $GOF = 53 \div 91$ ) for the velocities. The fit is also very good at AM2 (Fig. 11b) for the acceleration, even if the recorded displacements are underestimated with a poor fit and low GOF values; an



**Fig. 10** Boxplots of the 2.0 s PSV extracted, for each receiver, from the simulations of the four scenarios. Each box the red line is the median value, the box edges are the 1st and 3rd quartiles, while the ends of the whiskers are the lowest datum still within 1.5 interquartile range of the lower quartile, and the highest datum still within 1.5 IQR of the upper quartile. The outliers are plotted as (red) crosses. The shadowed area represents the GMPE by Akkar et al. (2014)  $\pm \sigma$





◀ **Fig. 12** Comparison between the recorded waveforms (*black lines*) and the EGF waveforms (*red lines*) computed for the **a** LOR and **b** AM2 and **c** MUL stations; the source adopted is Model D modified for the rupture propagation that is set as bilateral,  $\frac{1}{4}$  toward NE and  $\frac{3}{4}$  toward SW

analogous trend can be observed at MUL station (Fig. 11c), also located NE from the epicenter. Displacements are affected by low amplitudes at low frequencies because the  $M_w = 3.9$  element earthquake does not substantially contribute to them.

To improve the fit on the stations located NE of the seismic source, we modified the rupture directivity of the source model with a partially bilateral rupture (directivity ratio of 0.75) propagating for  $\frac{1}{4}$  of fault length toward NE and for  $\frac{3}{4}$  of fault length toward SW. In this case, the fit of the LOR data worsens (Fig. 12a) with respect to the previous rupture model with a fair fit in acceleration and displacement; however the fit of the other stations improves, and also at the stations AM2 (very good fit-Fig. 12b), and MUL (excellent fit - Fig. 12c) displacements are satisfactorily reproduced. In all cases, our synthetic seismograms underestimate the long period content observed on the signals recorded at ZAR.

## 5 Conclusions

To investigate the variability of ground motion related to the source model we computed the strong motion (up to 1 Hz) for the well-studied  $M_w$  5.2 Lorca earthquake applying a deterministic approach integrated with a kinematic source model. We first verified that no specific effects below 15 Hz, due to the particular site and the station deployment are present at LOR by performing 1-hour ambient noise recordings and analyzing H/V ratios.

The data recorded at LOR have been explained as strongly influenced by the seismic source directivity, and several fault models were published in the literature. Their main differences can be ascribed to the different input data used and to the different resolution power of the employed inversion techniques. For instance, the Lorca source model obtained from the inversion of seismological data is not fully constrained in the engineering frequency range because only a few near-source accelerometric records are available. Moreover, the geodetic signals are characterized by the long period content and do not help to constrain the source parameters at high resolution as already observed for other moderate earthquakes.

The comparisons between the simulations and the seismic recordings ( $f \leq 1$  Hz), as well as the synthetic PGV maps, show that the best fit is obtained using the source parameters of Model D, a model with a rupture propagating almost unilaterally from NE toward SW with a single slip patch concentrated between the nucleation and Lorca. Model D is also used to simulate the high-frequency ground motion by EGFs. We obtain an excellent fit for the recording at LOR, while we underestimate the motion recorded at stations AM2 and MUL, which are located NE from the epicenter and could be affected by backward directivity and/or local soil effects. Considering a bilateral rupture propagating asymmetrically ( $\frac{1}{4}$  of fault length toward NE), similar to the one proposed by López-Comino et al. (2012) and Martínez-Díaz et al. (2012), we improve the fit of the NE stations, and we obtain a good average simulation of HF motion all over the near-field area.

The ground motion variability observed for the 2011 Lorca earthquake, are certainly affected by the aleatory and the epistemic uncertainty in the source inversion process. In our modeling, the regional earth model, the timing of rupture propagation, as well as the technique used in the simulations are well constrained. Hence, the complexity of the earthquake rupture process (i.e. the maximum slip on the fault, the nucleation position on

the main slip area, and the position of the fault plane) has a significant influence on the near-field ground motion.

On average the 2 s PSV differences, spanning over one order of magnitude, are high close to the source while they decrease at larger distances (at more than 50 km away from the source), where the directivity effect becomes negligible, due to a combination of the rupture-propagation direction and the S-wave radiation pattern. Mena and Mai (2011) found that directivity pulses are primarily related to slip heterogeneity (i.e., the size and location of slip asperities). Moreover, when the slip is heterogeneous, the rupture velocity and the rise time, either homogeneous or heterogeneous, have weaker effects on the ground motion variability (Vyas et al. 2016).

The comparison of the ground motion variability with that from the GMPE shows a good accordance within  $\pm 1 \sigma$ , except for the very near-source station located above the rupture area (e.g. LOR) and the stations affected by forward directivity effects (e.g. VER, OLU). However, the bias in GMPE caused by the paucity of near-field records makes difficult the physical explanation of ground motion variability at those distances. This obviously suggests the need to increase the number of accelerometric stations in earthquake prone areas. Waiting for this to happen, it is of paramount importance to model the ground motion using well-established approaches that employ complex rupture process and wave propagation effects, in order to investigate the resulting ground motion variability and to improve the ground motion prediction for future earthquakes.

## 6 Data and resources

The waveforms are downloaded from the Instituto Geografico Nacional (IGN, Spain) website (<http://www.ign.es/ign/layoutIn/sismoFormularioAcelerogramas.do>). Software and code used: EGF code (courtesy of Hiroe Miyake) was used for time series reproduction, Seismic Analysis Code, SAC (<http://ds.iris.edu/files/sac-manual/>) was for waveform analysis and the Generic Mapping Tools (Wessell and Smith, 1991) for map reproduction. All sites were last accessed in December 2016.

**Acknowledgements** We kindly acknowledge P.J. González, J.J. Martínez-Díaz, and M.A. Santoyo for providing us with the digital model for their slip distribution associated with the 2011 Lorca earthquake; J.M. Alcalde Camino for the IGN accelerometric signals; J. Morales, IAG (University of Granada), for providing temporary seismic network data; L. Mendoza and J. Martín Dávila (ROA, Cadiz) for the GPS data. Special thanks to the Lorca City Council for support during the ambient-noise surveys. The Editor in Chief, Attila Ansal, and two anonymous reviewers are acknowledged for their constructive comments, which helped improve this article. Field work and ambient-noise analysis were partially supported by the Spanish Projects CGL2007-62454 and CGL2010-11831-E.

## References

- Akkar S, Sandikkaya MA, Bommer JJ (2014) Empirical ground-motion models for point- and extended-source crustal earthquake scenarios in Europe and the Middle East. *Bull Earthq Eng* 12:359–387
- Alguacil G, Vidal F, Navarro M, García-Jerez A, Pérez-Muelas J (2014) Characterization of the earthquake shaking severity in the town of Lorca during the May 11, 2011 event. *Bull Earthq Eng* 12:1889–1908
- Ameri G, Pacor F, Cultrera G, Franceschina G (2008) Deterministic ground-motion scenarios for engineering applications: the case of Thessaloniki, Greece. *Bull Seismol Soc Am* 98:1289–1303
- Anderson JG (2010) Source and site characteristics of earthquakes that have caused exceptional ground accelerations and velocities. *Bull Seismol Soc Am* 100:1–36

- Avouac JP (2012) Human-induced shaking. *Nat Geosci* 5:763–764
- Beltrán Díez A, Jiménez MJ, García-Fernández M, Amaral-Ferreira M, Sousa-Oliveira C, Mota de Sá F (2013) Impact assessment of the 2011 Lorca earthquake: QuakeIST seismic simulator approach. *Misc INGV* 21:39–40
- Cabañas L, Alcalde JM, Carreño E, Bravo JB (2014) Characteristics of observed strong motion accelerograms from the 2011 Lorca (Spain) Earthquake. *Bull Earthq Eng* 12:1909–1932
- Corchete V, Chourak M (2011) Shear-wave velocity structure of the south-eastern part of the Iberian Peninsula from Rayleigh wave analysis. *Int J Earth Sci* 100:1733–1747
- Frontera T, Concha A, Blanco P, Echeverría A, Goula X, Arbiol R, Khazaradze G, Pérez F, Suriñach E (2012) DInSAR coseismic deformation of the May 2011  $M_w$  5.1 Lorca earthquake (southeastern Spain). *Solid Earth* 3:111–119
- González PJ, Tiampo KF, Palamo M, Cannavò F, Fernández J (2012) The 2011 Lorca earthquake slip distribution controlled by groundwater crustal unloading. *Nat Geosci* 5:821–825
- Hartzell SH (1978) Earthquake aftershocks as Green's functions. *Geophys Res Lett* 5:1–4
- Irikura K (1986) Prediction of strong acceleration motion using empirical Green's function. In: Proceedings of 7th Japan earthquake engineering symposium, vol 151–156, Tokyo, 10–12 December 1986
- López-Comino J, Mancilla F, Morales J, Stich D (2012) Rupture directivity of the 2011,  $M_w$  5.2 Lorca earthquake (Spain). *Geophys Res Lett* 39:L03301
- Mai PM, Thingbaijam KKS (2014) SRCMOD—An online database of finite-fault rupture model. *Seismol Res Lett* 85:1348–1357
- Mai PM, Imperatori W, Olsen KB (2010) Hybrid broadband ground-motion simulations: combining long-period deterministic synthetics with high-frequency multiple S-to-S backscattering. *Bull Seismol Soc Am* 100:2124–2142
- Martínez-Díaz JJ, Bejar-Pizarro M, Álvarez-Gómez JA, Mancilla F, Stich D, Herrera G, Morales J (2012) Tectonic and seismic implications of an intersegment rupture. The damaging May 11<sup>th</sup> 2011  $M_w$  5.2 Lorca; Spain, earthquake. *Tectonophysics* 546–547:28–37
- McGuire JJ, Zhao L, Jordan TH (2002) Predominance of unilateral rupture for a global catalog of large earthquakes. *Bull Seismol Soc Am* 92:3309–3317
- Mena B, Mai PM (2011) Selection and quantification of near-fault velocity pulses owing to source directivity. *Georisk* 5:25–43
- Mendoza L, Kehm A, Koppert A, Martín Dávila J, Gárate J, Becker M (2012) The Lorca Earthquake observed by GPS: a test case for GPS seismology. *Física de la Tierra* 24:129–150
- Miyake H, Iwata T, Irikura K (2003) Source characterization for broadband ground-motion simulations: kinematic heterogeneous source model and strong motion generation area. *Bull Seismol Soc Am* 93:2531–2545
- Moratto L, Vuan A, Saraò A (2015) A hybrid approach for broadband simulations of strong ground motion: the case of the 2008 Iwate–Miyagi Nairiku earthquake. *Bull Seismol Soc Am* 105:2823–2829
- Mucciarelli M (2014) The role of site effects at the boundary between seismology and engineering: lessons from recent earthquakes. In: Ansal A (ed) *Perspectives on european earthquake engineering and seismology*. Springer, New York, p 179–194. ISBN 978-3-319-07117-610. DOI 1007/978-3-319-07118-3
- Navarro M, García-Jerez A, Alcalá FJ, Vidal F, Enomoto T (2014) Local site effect microzonation of Lorca town (SE Spain). *Bull Earthq Eng* 12:1933–1959
- Olsen KB, Mayhew JE (2010) Goodness-of-fit criteria for broadband synthetic seismograms, with application to the 2008  $M_w$  5.4 Chino Hills, California, earthquake. *Seismol Res Lett* 81:715–723
- Pro C, Buforn E, Cesca S, Sanz de Galdeano C, Udías A (2014) Rupture process of the Lorca (southeast Spain) 11 May 2011 ( $M_w = 5.1$ ) earthquake. *J Seismol* 18:481–495
- Ripperger J, Mai PM, Ampuero JP (2008) Variability of near-field ground motion from dynamic earthquake rupture simulations. *Bull Seismol Soc Am* 98:1207–1228
- Rivas-Medina A, Martínez-Cuevas S, Quiros LE, Gaspar-Escribano JM, Staller A (2014) Models for reproducing the damage scenario of the Lorca earthquake. *Bull Earthq Eng* 12:2075–2093
- Rueda J, Dreger D, García Blanco RM, Mezcua J (2014) Directivity detection and source properties of the 11 May 2011  $M_w$  5.2 Lorca, Spain, earthquake. *Bull Seismol Soc Am* 104:1735–1749
- Santoyo MA (2014) Finite fault analysis and near-field dynamic strain and rotation estimates due to the 11/05/2011 ( $M_w$  5.2) Lorca earthquake, south-eastern Spain. *Bull Earthq Eng* 12:1855–1870
- Spudich P, Frazer LN (1984) Use of ray theory to calculate high frequency radiation from earthquake sources having spatially variable rupture velocity and stress drop. *Bull Seismol Soc Am* 74:2061–2082
- Spudich P, Xu L (2003) Documentation of software package Compsyn svx3.11: programs for earthquake ground motion calculation using complete 1-d Green's functions. In: Lee et al. (ed) *International handbook of earthquake and engineering seismology*, vol 2. Academic Press, New York

- Tinti E, Fukuyama E, Piatanesi A, Cocco M (2005) A kinematic source-time function compatible with the earthquake dynamics. *Bull Seismol Soc Am* 95:1211–1223
- Vyas JC, Mai PM, Galis M (2016) Distance and azimuthal dependence of ground-motion variability for unilateral Strike-Slip ruptures. *Bull Seism Soc Am* 106:1584–1599
- Wessell P, Smith WHF (1991) Free software helps map and display data. *Eos Trans Am Geophys Union AGU* 72:441